THE JOURNAL OF PHYSICAL CHEMISTRY C

Article

pubs.acs.org/JPCC

Molecular Dynamics Simulations of Supported Pt Nanoparticles with a Hybrid Sutton−Chen Potential

Fernando D. Vila,* Scott T. Hayashi, Jeffrey M. Moore, and John J. Rehr

Department of Physics, University of Washington, Seattle, Washington 98195, United States

Supporting Information

ABSTRACT: Understanding the physical and chemical behavior of supported nanoscale catalysts is of fundamental and technological importance. However, their behavior remains poorly understood, in part due to their complex, dynamical structure and the nature of interactions at the nanoscale. We found previously that real-time ab initio finite temperature DFT simulations provide fundamental insights into the dynamic and electronic structure of nanoparticles. Unfortunately, such first-principles calculations are very computationally intensive. To make such simulations more feasible, we have developed a hybrid version of the classical Sutton−Chen model potential which is orders of magnitude more efficient. This potential is parametrized to previous DFT/MD simulations and accounts for many-body effects induced by the support. The model is applied to $Pt_{10,20}$ nanoparticles supported on a model γ-Al_2O_3 surface. In addition to the thermal variation of the internal structure, the model also predicts diffusion coefficients and bond-breaking rates. The simulations reveal size-dependent dynamical changes with increasing temperature, as the clusters go from a "frozen" state attached to the support, to a "liquid" state where they are free to diffuse. These changes provide a rationale for the observed negative thermal expansion. Implications for nanoscale catalysis are briefly discussed.

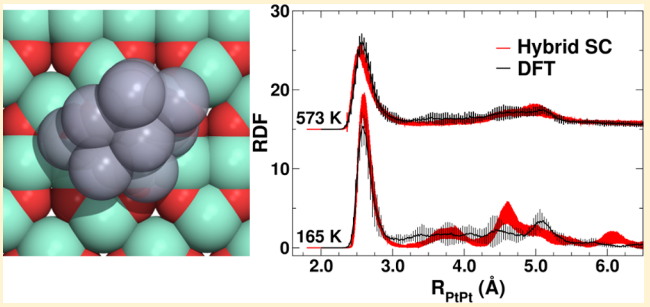

1. INTRODUCTION

Metallic nanoclusters are attractive candidates for dispersed catalysts for many important reactions. This is due, in part, to their increased surface to volume ratio compared to bulk materials and also to their heterogeneous structure, both of which allow for increased selectivity in chemical reactions.[1] Consequently, nanocatalysis has been one of the oldest applications of nanoscience[1] and has been in wide use for a range of industrial applications, including catalytic conversion of vehicle emissions and petroleum reforming.[2] Nevertheless, owing to their complex, dynamic structure, and the nature of interatomic interactions at the nanoscale, the mechanisms of nanocatalysis are still not well understood. These properties are often studied using X-ray spectroscopy (XAS) techniques, and previous XAS experiments have reported that oxide-supported Pt_{10} nanoparticles display a variety of anomalous characteristics, such as large structural disorder, negative thermal expansion (NTE), and thermally induced changes in electronic structure.[3] Density functional theory/molecular dynamics (DFT/MD) calculations have been used to investigate these systems, and have successfully explained many of these phenomena. Indeed ab initio, finite temperature DFT/MD calculations are well-suited for exploring the dynamical nature of these systems.[4]

Unfortunately, first-principles DFT/MD calculations in nanoscale systems can be impractical in terms of sheer computational demand, scaling roughly as $N^3 \times N_T$, where N is the size of the system and N_T the number of time-steps in the calculation. Typically N including a model support is of order 10^2 while N_T is of order 10^4, assuming time steps of a few fs and runs of many ps. Thus, the net phase-space accessibility of a system becomes largely dependent on the affordability of computational resources. Previous DFT/MD calculations of Pt_{10} nanoclusters have typically required of order 10^3 CPU hours per ps.[5] Thus, calculations of physical quantities requiring long relaxation times, such as diffusive properties and long-period thermal fluctuations can be prohibitive.

In an effort to ameliorate these limitations, we have developed a classical model potential for classical molecular dynamics simulations with parameters tuned to nanoscale systems. We aim to offer a practical alternative to ab initio molecular dynamics (AIMD) of Pt nanoparticles of sizes commonly used in research and industry, i.e., with tens to hundreds of atoms. Our approach generalizes the model potential introduced by Sutton and Chen (SC), which includes density-dependent many-body terms,[6] by modifying the Pt−Pt interaction for nanoscale clusters that includes the interaction with the support. The original SC potential was tailored for bulk fcc transition metals; it has been shown to accurately model long-range van der Waals pair interactions and to approximate the many-body metallic bonding of the crystal.[7] This original potential has been successfully applied in many bulk studies and gives reasonable agreement with experiment.[8]

Received: March 24, 2016
Revised: June 20, 2016
Published: June 21, 2016

DOI: 10.1021/acs.jpcc.6b03074
J. Phys. Chem. C 2016, 120, 14883−14891

Table 1. Parameters for the Augmented and Hybrid SC Potentials Used in This Paper

potential		ϵ (eV)	a/a' (Å)	c/b	n/n'	m/m'	σ (Å)	k_{OAl} (eV/Å^2)
aug.	U^{SC}_{PtPt}	0.0098721	3.9163	70.743	11	7		
	U^{LJ}_{PtO}	0.228					1.866	
	U^{LJ}_{PtAl}	0.044					2.420	
	U^{H}_{OAl}							6.0
hyb.	U^{SC}_{PtPt}	0.01832262	3.4075	25.9591	14	11		
	U^{SC}_{PtO}		1.0380	70.4246	12	12		
	U^{LJ}_{PtO}	0.4104					1.866	
	U^{LJ}_{PtAl}	0.044					2.420	
	U^{H}_{OAl}							6.0

More importantly, for the purposes of our model the potential enables calculations that are orders of magnitude faster than AIMD. The speed of our classical MD calculations now allows us to probe very long time evolutions of many different nanoscale systems. Furthermore, the parametrized form of the potential provides a flexibility for the model, allowing the potential to be adjusted to a given system. To assess the performance of the new parametrization we compare our results for the pair distribution functions to those obtained with the original SC model and to previous AIMD calculations. In addition, we have studied slow-converging properties such as autocorrelation functions, temperature-dependent diffusivities, and bond-breaking properties. These simulations allow us to provide a detailed picture of the structure and long-time behavior of nanoparticles of various sizes as a function of temperature.

The paper is organized as follows: In section 2.1 we present a detailed description of the modifications made to the original SC potential to account for the presence of the support. Sections 2.2 and 2.3 describe the process and references used for the reparametrization, as well as computational details of the different simulations. Section 3 presents our results, including the figures of merit of the new model potential, structural properties, and diffusive properties. Finally, section 4 presents our conclusions and possible improvements to the model potential.

2. METHODOLOGY

2.1. SC Potentials for Nanoparticles. It is widely appreciated that the effective interaction between pairs of atoms or molecules depends on their local environment. For example, intermolecular model potentials for water based on monomer or dimer properties tend to give good results for small clusters, but poorly characterize liquid or solid properties.[9] Pt clusters also show such environmental effects, with significant many-body interactions that change the effective Pt−Pt bonding as a function of nanoparticle size.[10,11] For these reasons, the original parametrization of the SC potential, which was designed to reproduce properties of bulk fcc Pt, is inappropriate to describe the heterogeneous bonding in nanoclusters, and a new parametrization is needed. To accomplish this we first augmented the original SC potential with pair interactions to the support. However, we found that this change alone fails to provide good agreement with reference AIMD results. Therefore, we next changed the SC parametrization without altering the functional form of the potential. Although this yielded improved radial distribution functions, they were still qualitatively different from the AIMD ones. Finally we developed a hybrid model potential that uses both a new SC parametrization and potential form together with terms that account for the many-body cluster-support interactions. We find that this hybrid model gives results that compare well with those from AIMD, yet are orders of magnitude more efficient computationally.

2.1.1. Augmented SC Model. Our augmented model potential U consists of three terms: a standard SC model U^{SC} for the Pt atom cluster, a Lennard-Jones (LJ) model for the interaction between the cluster and the support U^{LJ}, and a simple Harmonic potential U^{H} that characterizes the fluctuating structure of the support at a given temperature

$$U = U^{SC} + U^{LJ} + U^{H} \tag{1}$$

The SC potential has the usual form in terms of a two-body power-law repulsive part U^{R} and a density dependent attractive part U^{A}, i.e.:

$$U^{SC}_{PtPt} = U^{R}_{PtPt} + U^{A}_{PtPt} \tag{2}$$

$$U^{R}_{PtPt} = \frac{\epsilon}{2} \sum_{\substack{i \neq j \\ i,j \in Pt}} \left(\frac{a}{r_{ij}}\right)^{n} \tag{3}$$

$$U^{A}_{PtPt} = -c\epsilon \sum_{i \in Pt} \sqrt{\rho_i} \tag{4}$$

Here the so-called "density" term ρ_i which is strongly dependent on the local environment of a given pair, is defined as

$$\rho_i = \sum_{\substack{j(\neq i) \\ j \in Pt}} \left(\frac{a}{r_{ij}}\right)^{m} \tag{5}$$

The interaction between the Pt atoms in the nanocluster and the X = {Al, O} atoms of the γ-alumina support is described by standard 12-6 LJ potentials of the form

$$U^{LJ}_{PtX} = 4\epsilon^{LJ}_{PtX} \sum_{\substack{ij \\ i \in Pt/j \in X}} \left[\left(\frac{\sigma_{PtX}}{r_{ij}}\right)^{12} - \left(\frac{\sigma_{PtX}}{r_{ij}}\right)^{6}\right] \tag{6}$$

Finally the fluctuating substrate with equilibrium coordinates $\mathbf{r}^0$ is characterized by a simple quasi-harmonic potential

$$U^{H}_{OAl} = \frac{1}{2} \sum_{r_{OAl} \in NN} k_{OAl} |r_{OAl} - r^{0}_{OAl}|^2 \tag{7}$$

In our augmented SC potential, the parameters for U^{SC} are fixed to be the same as in the original SC parametrization, as shown in Table 1.[6] The U^{LJ} parameters were obtained by fitting the near-neighbor Pt-X radial probability distribution functions

DOI: 10.1021/acs.jpcc.6b03074
J. Phys. Chem. C 2016, 120, 14883−14891

against DFT/MD simulations (described in detail in section 2.3.1) with a temperature dependent radial distribution

$$P(R_{PtX}) = \frac{1}{Z} e^{-U^{LJ}_{PtX}/kT} \quad (8)$$

where $Z = \int_0^\infty dR_{PtX}\ e^{-U^{LJ}_{PtX}/kT}$. The parameters used are discussed in detail in section 2.2 for the final form of the potential described in section 2.1.3.

Figure 1 shows the Pt−Pt radial distribution functions (RDFs) for supported Pt_{10} at 165 and 573 K, obtained with this

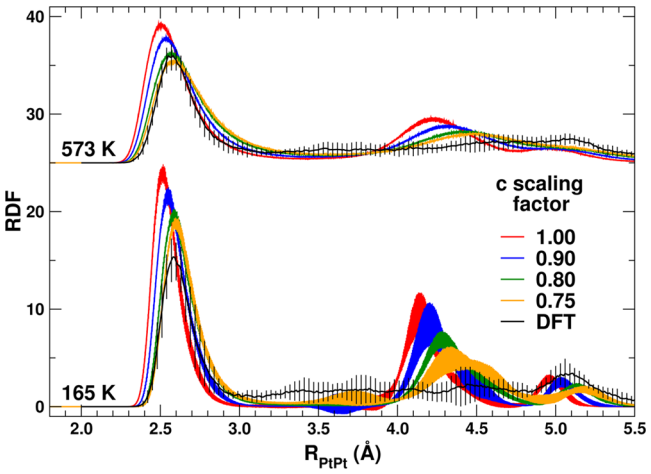

Figure 1. Comparison of the DFT/MD and SC radial distribution functions of Pt_{10} at 165 and 573 K as a function of the scaling factor of the SC c parameter. The unscaled red curves correspond to the original SC parametrization.[6]

augmented potential (red curves) compared to the DFT/MD results (black curves). Clearly, the original SC parameters result in too tight Pt−Pt binding in nanoparticles of this size as demonstrated by the narrow and left-shifted first shell peak (2.4−2.9 Å). Moreover, the DFT/MD simulations show different behavior at low (165 K) and high (573 K) temperature: Although not completely rigid, at 165 K the cluster has a well-defined structure characterized by a combination of static and vibrational disorder. At 573 K, however, the Pt_{10} cluster is mostly melted and dominated by so-called "dynamic structural disorder" (DSD), with no well-defined second shell. This differential behavior is not present in the model potential simulations. The SC results show a pronounced feature between 4.0 and 4.5 Å, reminiscent of the second and third shells present in the metal between 3.9 and 4.8 Å. In addition, visual inspection of the SC MD trajectories reveals clusters that are largely rigid even at 573 K. Therefore, we proceed to change the original parameters to improve the results for these nanoparticles.

2.1.2. Reparametrization of the Augmented SC. In this section we modify the SC parametrization while keeping the original form of the potential. Excluding the n and m exponents, the SC potential has only three parameters that can be modified in order to change the Pt−Pt RDF: the energy scaling factor ϵ, the lattice parameter a, and the unitless constant c. It should be noted here that changing the Pt−O and Pt−Al LJ potentials has very little effect on the Pt−Pt RDF, as discussed in more detail in the next section. Changes to the SC energy parameter ϵ preserve the relative weights of the attractive and repulsive parts of the potential, thus mostly only affecting the shape of the first shell peak and leaving the RDF roughly unchanged. Similarly, the SC lattice constant a does not affect the balance or attraction and repulsion, acting only as a space-scaling parameter which shifts the position of the peaks in the RDF while preserving their overall shapes. The c parameter in eq 4, on the other hand, can be used to change the relative strength between the attractive and repulsive parts of the potential, thus is a good candidate for reparametrization. Figure 1 shows the effect of scaling c down to 75% of its original value. Clearly, making the attractive part of the potential weaker results in both a shift of the first shell as well as a damping of the secondary structure. At 573 K the qualitative agreement between the SC and DFT/MD RDFs is greatly improved. The most noticeable disagreements are in the width of the first shell, the position of the broad "second shell" feature, and the lack of bonds at intermediate lengths between the first and second shell features. The reparametrized SC potential produces a wider first shell and consequently larger Pt−Pt mean square relative displacement (MSRD), indicating that the softening of the attractive part makes the effective pair potential too soft. In contrast, the lack of intermediate bonds indicates that the nanoparticle largely preserves its structure and is not as dynamic as in the DFT/MD simulations. This overstructuring of the potential is even more glaring at 165 K, where the RDF shows a well-defined second shell, in contrast with the DFT/MD simulations. Given these results it is clear that more flexibility needs to be introduced into the SC form to account for both the interaction with the support and the change in effective Pt−Pt interaction in the nanoparticles vs in the solid.

2.1.3. Hybrid SC Potential. To account for these many-body effects induced by the presence of the support, we introduce a new, hybrid expression for the total potential energy of the system by replacing the original U^{SC} form in eq 2 as follows:

$$U^{SC}_{PtPtO} = U^{R}_{PtPt} + U^{A}_{PtPtO} + U^{R}_{PtO} \quad (9)$$

Here U^{R}_{PtPt} is the same as in eq 3. U^{A}_{PtPtO} is a new attractive part that modulates the Pt−Pt interaction as a function of the interaction with the oxygen atoms in the support. This term has the familiar form shown in eq 4 but with an embedded atom ρ_i redefined as follows

$$\rho_i = \sum_{\substack{j(\neq i)\\ j\in Pt}} \left(\frac{a}{r_{ij}}\right)^m + \sum_{j\in O} \left(\frac{a'}{r_{ij}}\right)^{m'} \quad (10)$$

The first term of eq 10 accounts for the attractive interaction between Pt atoms and has the overall effect of weakening a Pt−Pt bond as a function of the number of Pt atoms that surround it. Previous ab initio simulations have shown that the same weakening is expected in the presence of the support.[5,12,13] Therefore, the second component in eq 10 was introduced to account for the interaction with the oxygen atoms. Finally, the U^{R}_{PtO} term, defined as

$$U^{R}_{PtO} = b\epsilon \sum_{\substack{ij\\ i\in Pt/j\in O}} \left(\frac{a'}{r_{ij}}\right)^{n'} \quad (11)$$

must be included to account for the attractive Pt−O interaction introduced in eq 10.

The rest of the potential remains similar to that in the augmented SC form in eq 1, albeit with modified parameter

DOI: 10.1021/acs.jpcc.6b03074
J. Phys. Chem. C 2016, 120, 14883−14891

Table 2. Comparison of the NN_{Pt}, $\langle R_{PtPt}\rangle$ (in Å), and σ^2_{PtPt} (in Å^2) from DFT/MD Simulations and the New Hybrid SC Form, as a Function of Cluster Size and Temperature (in K)[a]

		NN_{Pt}		$\langle R_{PtPt}\rangle$		σ_{PtPt}^2	
cluster	temp.	DFT/MD	hyb. SC	DFT/MD	hyb. SC	DFT/MD	hyb. SC
Pt_{10}	165	3.7(5)	4.0(3)	2.623(28)	2.627(14)	0.011(3)	0.009(09)
Pt_{10}	573	3.2(3)	3.0(2)	2.618(28)	2.609(16)	0.016(3)	0.019(16)
Pt_{20}	165	4.4(2)	5.1(7)	2.649(16)	2.671(26)	0.010(2)	0.012(15)
Pt_{20}	573	4.5(2)	3.7(3)	2.676(11)	2.651(19)	0.020(3)	0.024(26)

[a]Values in parentheses indicate the error in the last significant figures.

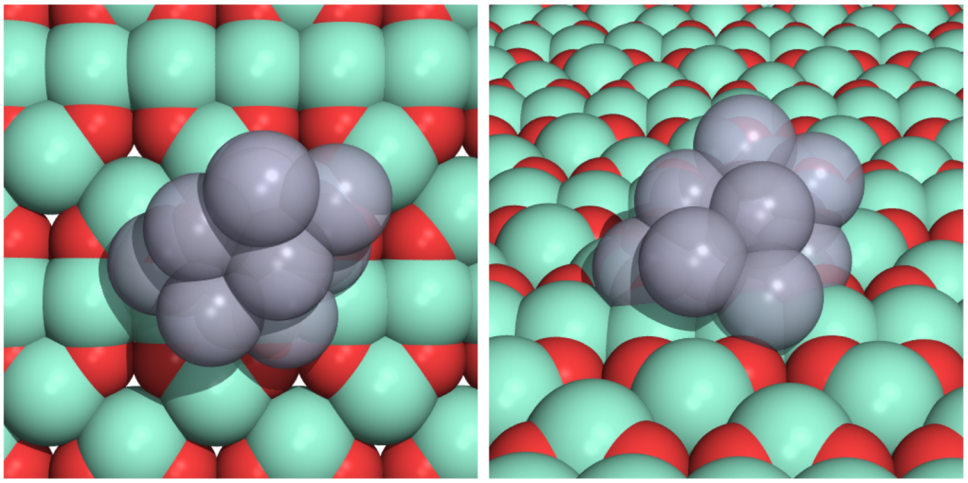

Figure 2. Top and side view of a snapshot from a typical Pt_{10} simulation at 200 K.

values. The U^{LJ}_{PtX} term now accounts for the pair Pt−O interactions not included in U^{SC}_{PtPtO}, while the U^{H}_{OAl} harmonic term is the same as in section 2.1.2.

2.2. Parameter Optimization. Given that our main objective is to replace computationally demanding ab initio simulations by efficient model potential ones, we base our new parametrization on DFT/MD results. These results have been successful in reproducing semiquantitatively many of the unusual properties of supported Pt clusters. To obtain the parameters needed for the new SC form described in the previous section we first generate well-converged reference ab initio Pt−Pt, Pt−O and Pt−Al radial distribution functions using DFT/MD simulations (see next section for details). Then we perform MD simulations using the hybrid SC form for different parameter sets, with the aim of matching three key figures of merit (FOMs) between the ab initio and model RDFs of Pt_{10}. We leave Pt_{20} out of the process to provide a measure of the quality of the parametrization. The chosen FOMs determine the nature of the first Pt coordination shell, and are (i) the number of Pt near-neighbors $\overline{NN}_{Pt}$ around a Pt atom, (ii) the mean Pt−Pt bond distance $\overline{R}_{PtPt} = \langle R_{PtPt}\rangle$, and (iii) the Pt−Pt mean square relative displacement (MSRD) $\sigma^2_{PtPt} = \langle (R_{PtPt} - \overline{R}_{PtPt})^2\rangle$. Given that we are optimizing the new parameters to properties in small nanoparticles, we do not expect the final hybrid potential to be transferrable to either unsupported systems or the bulk.

In order to provide fast an reliable screening of possible parameter sets, the FOMs were obtained by automatically fitting the first shell to a composite function of two Gaussians with different width, one for the region below the RDF maximum and one for that above it. The parameters for the fitting Gaussians were obtained by matching their centers and widths to the maximum and half-maxima on each side of the distribution, respectively. Then the distribution generated by this composite can be easily integrated to obtain the FOMs. To minimize sampling effects, in particular at low temperatures, the FOMs are computed from RDFs averaged over twenty MD runs with different initial conditions. Parameter sets with good FOMs compared to the ab initio values were found by scanning the parameter space. The final set of parameters is shown in Table 1, while the corresponding FOMs are presented in Table 2. It should be noted that these final FOMs were computed by manually fitting a skew-normal distribution to the first coordination shell as was done in ref 12 since this provides slightly more accurate results.

2.3. Computational Details. *2.3.1. Reference DFT/MD Simulations.* The Pt_{10} and Pt_{20} ab initio DFT/MD runs on γ-Al_2O_3 were performed using VASP[14] at 165 and 573 K using the Nosé−Hoover thermostat. All simulations were non-relativistic, performed with spin-unpolarized densities at the Γ point, using the PBE functional, ultrasoft pseudopotentials, and a plane wave cutoff of 297 eV. Six initial structures were generated for each temperature by creating random spherical clusters with appropriate bond distances (2.5−2.9 Å). These clusters were then placed onto the "d" layer of the dehydroxylated [110] surface of γ-Al_2O_3 and fully optimized before starting the MD simulations. The γ-Al_2O_3 surface is represented by four layers (two fully relaxed and two frozen) in a slab of 19.4 Å × 13.7 Å with an effective vacuum separation of 16 Å. All simulations used the velocity-Verlet integration method with a 3 fs time step, which is adequate to capture the fastest structural fluctuations in the system at these temperatures. After an initial 6 ps thermalization period, statistical averages were acquired for 10 ps.

2.3.2. Model Potential Simulations. Simulations were carried out for Pt_{10} and Pt_{20} nanoclusters on a simplified

DOI: 10.1021/acs.jpcc.6b03074
J. Phys. Chem. C 2016, 120, 14883−14891

single-layer [110] surface of γ-Al_2O_3 (Figure 2) over a range of temperatures between 50 and 700 K, at 50 K intervals. All simulations were performed with software developed on-site by the authors. Total simulation lengths of 100 ps were used, with an initial thermalization of 10 ps, and a time step of 1 fs. This is shorter than the time step used in the ab initio MD simulations due to the higher temperatures investigated with the hybrid model potential. Initial configurations for the clusters were selected from a seeding run at 1000 K. Twenty initial configurations were used for each cluster size and at each temperature. Unless otherwise noted, all error bars shown in this paper correspond to standard deviations obtained from these initial conditions. The initial velocities of the atoms were randomized with a normal distribution and rescaled to produce kinetic energies corresponding to the desired temperature. The simulations used the velocity-Verlet algorithm with a Nosé–Hoover thermostat to evolve the system in time at constant temperature. The τ parameter of the Nosé–Hoover thermostat was chosen to be 0.1 ps. This value ensures that the thermostat remains thermally coupled to the system.

As currently implemented, our hybrid model potential calculations scale as $O(N_{Surf} \times N_{Pt})$, where N_{Surf} is the total number of atoms in the surface and N_{Pt} the number of Pt atoms, indicating that the simulations are dominated by the computation of the interaction between the cluster and the surface. This is due to the fact that the intrasurface interaction is only between near-neighbors, and that usually $N_{Surf} \gg N_{Pt}$, resulting in a negligible intracluster contribution to the scaling. It should be noted that better scaling could be achieved by implementing smart cutoffs, effectively reducing N_{Surf}. This scaling should be compared with the typical $O(N^3)$ with total number of atoms N in a DFT simulation. Although the scaling of the hybrid model potential is better than the DFT, the real power of the model resides in its much faster single-step timings. We find that on a single computing core each step in typical DFT simulations of supported Pt_{10} takes about 980 s. On the other hand, each step for an equivalent hybrid SC simulation takes only 2.8 ms, resulting in a speedup of 3.5×10^5.

3. RESULTS AND DISCUSSION

3.1. Many-Body Effects. To reveal the effects of many-body interactions we have computed $\overline{V}^N_{PtPt}$, the average effective pair potential as a function of the total number of neighbors N surrounding a Pt–Pt pair. This potential is defined as

$$\overline{V}^N_{PtPt}(R_{ij}) = \left\langle \frac{1}{T_{P_N}} \sum_{i,j \in P_N}^{T_{P_N}} U(\vec{R}_i, \vec{R}_j, \{\vec{R}_k(t)\}) \right\rangle_t \qquad (12)$$

where T_{P_N} is the number of Pt atom pairs in P_N, the set of pairs with a total number of neighbors N, i and j are atoms in this set, while k represents all remaining atoms. U is the energy of the system when the atoms are in positions $\vec{R}_i$, $\vec{R}_j$, and $\{\vec{R}_k(t)\}$, and $\langle\rangle_t$ indicates an average over configurations at different times in the MD trajectory. To build the potential curves, the positions of the i and j target atoms are $\vec{R}_i = \vec{R}_i(t) - x\vec{v}_{ij}$ and $\vec{R}_j = \vec{R}_j(t) + x\vec{v}_{ij}$, with $\vec{v}_{ij}$ a unit vector from $\vec{R}_i(t)$ to $\vec{R}_j(t)$, and x such that R_{ij} varies smoothly between 2.3 and 3.1 Å. Therefore, the potential curves are created by sampling a trajectory for structures and then computing the energy of the system as an embedded bond expands and contracts, while keeping the rest of the structure fixed. Figure 3 presents the $\overline{V}^N_{PtPt}$ potentials for Pt_{10} from a trajectory at 573 K. We find that the augmented and hybrid SC potentials have shifted distributions of the number of near-neighbors around each pair, with the augmented peaking at higher numbers than the hybrid. This is consistent with the previously discussed overbinding of the augmented parametrization. Thus, we only show the common results. The potentials show both the expected contraction of the bond and the increase of the force constant associated with less embedding of the atom pairs. At the extreme of an isolated, unsupported Pt dimer, potentials computed with the augmented and hybrid SC potentials, the DFT approach used in our MD simulations, and the CCSD(T) method, show the maximum extent of the bond contraction (Figure S1), with much lower Pt–Pt distances between 2.35 and 2.40 Å. The augmented SC with the original parametrization retains the underestimation of the force constant found for the metal (red vs blue curves), which results in RDFs that are too broad.

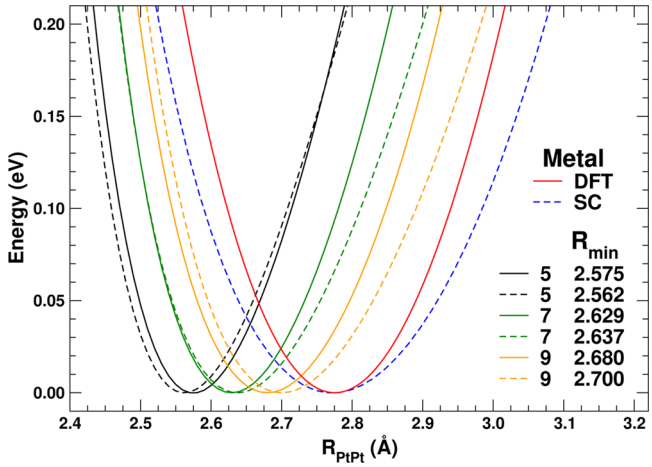

Figure 3. Average effective Pt–Pt pair potential for Pt_{10} as a function of the number of near neighbors surrounding the pair (for clarity only 5, 7, and 9 are shown). For comparison we also include the effective pair potential for the fcc metal computed with DFT (red) and the original SC potential (blue). The solid curves correspond to calculations with the hybrid SC potential while the dashed ones use the original parametrization. Notable are both the changes in minima R_{min} and effective bond strengths, with longer bonds characterized by larger coordination numbers. The averaging was done over structures extracted from single trajectories at T = 573 K.

3.2. Figures of Merit. The FOMs obtained with the chosen parameter set are presented in Table 2. Overall, all Pt_{10} FOMs are in good agreement with the DFT/MD reference results. The errors for the Pt_{20} FOMs are larger, not surprisingly given that they were not used in the parametrization, yet they are within the range of variation of the DFT/MD results. The change with increasing temperature of all three FOMs is somewhat overestimated by the hybrid SC model potential. This is likely due to a slightly overstructured near-neighbor shell at low temperature which becomes understructured at high temperature. This is noticeable in the case of the NN_{Pt}, which are somewhat too high at low temperature and too low at high temperature, and the MSRDs, which vary in the opposite direction. These trends are further discussed in the next Section.

3.3. Internal Structure and Dynamics. Beyond the FOMs of the near-neighbor shell, we can obtain a more detailed picture of the internal structure of the nanoclusters from their RDFs. Figure 4 shows the RDFs of Pt_{10} and Pt_{20} computed

DOI: 10.1021/acs.jpcc.6b03074
J. Phys. Chem. C 2016, 120, 14883–14891

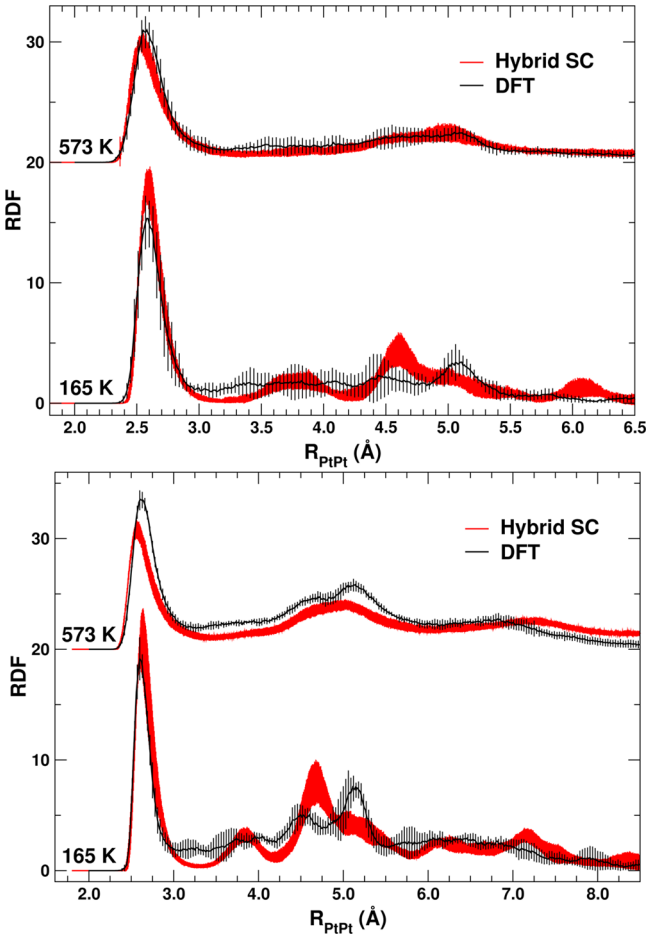

Figure 4. Radial distribution functions for Pt_{10} (top) and Pt_{20} (bottom) at 165 and 573 K obtained using the hybrid SC form with the parameters shown in Table 1. Figures of merit for these RDFs are summarized in Table 2.

with the hybrid SC reparametrization. Overall, they are in reasonable agreement with the DFT/MD RDFs, and most of the drawbacks of the original SC parametrization, highlighted in section 2.1.2 and Figure 1, are reduced or eliminated. First, the near-neighbor Pt−Pt bonds are no longer underestimated, with the first shell appearing in the correct position (as already demonstrated by the good agreement in the FOMs). Second, the distinct behavior at low (165 K) and high (573 K) temperature is now well reproduced. At low temperature the clusters show well-defined second and third shells in the correct range of 4.0 to 4.5 Å, while at high temperature they show the expected broad feature between 4.5 and 5.5 Å. More importantly, the region between the first and second shells now shows a significant population of Pt−Pt bonds, in contrast with the original SC parametrization. This population is associated with partial melting and DSD, as revealed by visual inspection of the MD trajectories. These show dynamic bond breaking and reforming within the nanocluster, and between the cluster and the support, with large vibrational motion between surface-bonded and nonsurface-bonded atoms. The cluster experiences sizable center of mass fluctuations which scale with increasing temperature, resulting in translation across the surface at high temperatures, a behavior that was mostly absent in simulations with the original parameters. To visualize this change more clearly, Figure 5 shows the RDF of Pt_{10} as a function of temperature. Here, the second and third shells are

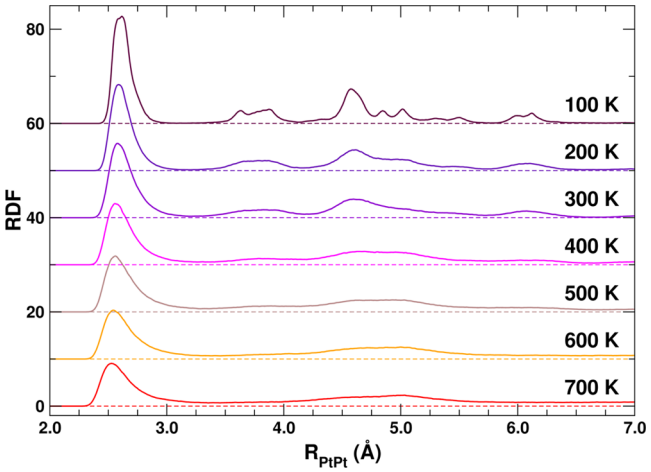

Figure 5. Radial distribution function for Pt_{10} as a function of temperature calculated with the new hybrid SC potential. The RDFs are averaged over 20 trajectories, each with randomized initial cluster configurations. At low temperature, the RDFs exhibit structured second and third Pt−Pt coordination shells. The attenuation of these shells with increasing temperature is indicative of the melting of the structure. Also noticeable is the left-shift of the first shell peak associated with NTE.

highly structured at 100 K. This structure remains up to ∼300 K and mostly disappears above that. We can also see that the bonds present in the intershell region at high temperatures are formed by the melting of the low-temperature second shell and its merging with the tail of the first shell. Finally, the negative thermal expansion (NTE) that is a signature of these small clusters[5] is visible as a left-shift of the near-neighbor shell.

Figure 6 shows the change in $\langle R_{PtPt} \rangle$ for Pt_{10} and Pt_{20} as a function of temperature. For Pt_{10} the NTE from 165 to 573 K

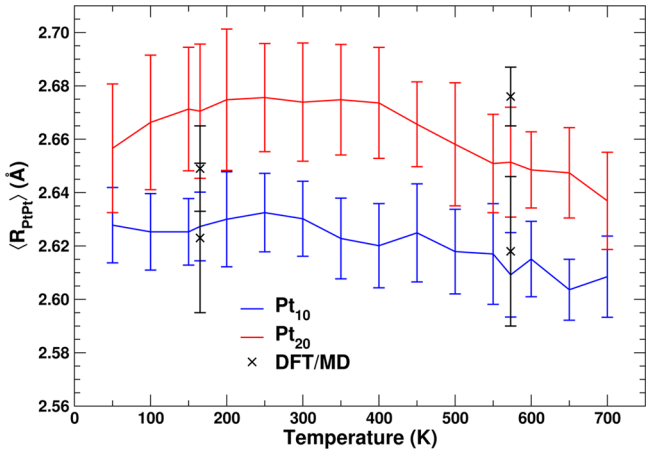

Figure 6. Mean Pt−Pt distance $\langle R_{PtPt} \rangle$ for Pt_{10} and Pt_{20} as a function of temperature calculated with the new hybrid SC potential.

is −0.018 Å, in better agreement with the −0.027 Å observed in experiment[3] than the −0.005 Å predicted by the DFT/MD simulations. Although both cluster sizes show NTE, the onset of contraction occurs at ∼300 K for Pt_{10} and ∼400 K for Pt_{20}, showing a similar behavior to other simulations.[15] Moreover, while the bond distance is approximately constant for Pt_{10} below the contraction onset, for Pt_{20} there is a region of positive thermal expansion (PTE) below ∼200 K. These different behaviors offer clues as to the origin of NTE which

DOI: 10.1021/acs.jpcc.6b03074
J. Phys. Chem. C 2016, 120, 14883−14891

will be discussed in detail in section 3.4. Briefly, we believe the onset of NTE is associated with the onset of diffusion of the nanoparticles over the support, while the positive expansion plateau is correlated to their internal melting.

Figures 7 and 8 show respectively the variation of NN_{Pt} and σ^2_{PtPt} as a function of temperature for both Pt_{10} and Pt_{20}. While

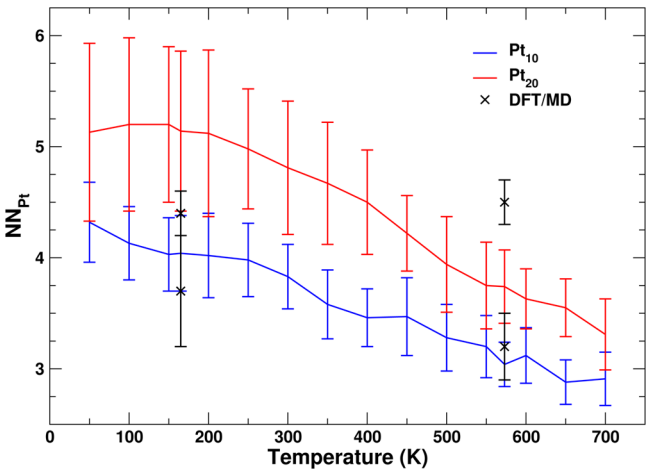

Figure 7. Number of Pt near-neighbors NN_{Pt} for Pt_{10} and Pt_{20} as a function of temperature calculated with the new hybrid SC potential.

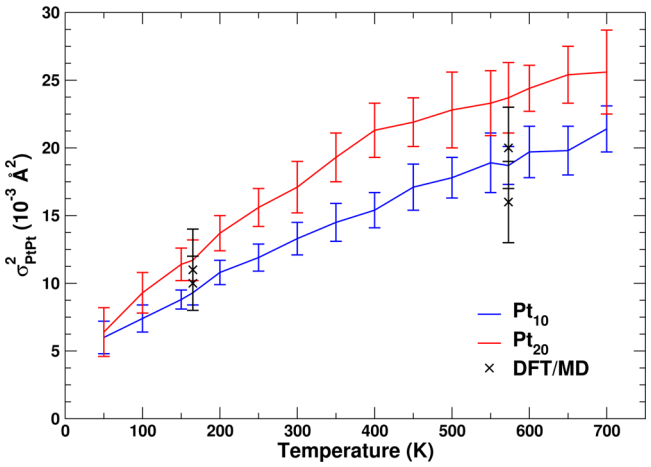

Figure 8. Mean-square relative displacement σ^2_{PtPt} for Pt_{10} and Pt_{20} as a function of temperature calculated with the new hybrid SC potential.

for Pt_{10} the number of near-neighbors decreases steadily as the temperature rises, for Pt_{20} NN_{Pt} is constant in the region below ~200 K, i.e., the region associated with the $\langle R_{PtPt}\rangle$ PTE. The σ^2_{PtPt} show a monotonic increase for both cluster sizes, but in Pt_{20} the expected linear behavior in the classical region above the Einstein temperature (177−230 K)[16] appears to be broken into two regions. Bilinear fits place the transition at the same temperature of ~400 K as the onset of NTE. Although not as noticeable, the bilinear fits also indicate a break in linearity for Pt_{10} at about 330 K. The regions above and below these onsets can be fit to the high temperature limit form of the MSRD, $\sigma^2_H = \sigma^2_0 + (\hbar^2 T)/(\mu k_B \Theta^2_E)$. Here σ^2_0 is the static disorder component, μ is the reduced mass of a Pt−Pt bond, and Θ_E is the Einstein temperature. We find that above their corresponding onsets, Pt_{10} and Pt_{20} have Einstein temperatures of 166 and 180 K, respectively, both close to the bulk metal value of 177 K. Their static disorders σ^2_0, however, are 9×10^{-3} and 15×10^{-3} Å^2, i.e., between 1 and 2 orders of magnitude larger than those usually measured for the solid metal.[16] These amounts of static disorder are consistent with those observed in liquid and amorphous systems.[17] In contrast, below threshold the clusters show amounts of static disorder (~5×10^{-3} Å^2) which are in reasonable agreement to those observed for nanoparticles of their size, which vary between 4−7 $\times 10^{-3}$ Å^2.[16] In this regime the Einstein temperature for Pt_{10} is 134 K, while for Pt_{20} is even lower at 110 K. Although the higher Θ_E at higher temperature might appear counterintuitive at first sight, the increase is associated with the shortening of the Pt−Pt bonds which get stiffer as they contract.

3.4. Diffusive Properties. It has been suggested[12,13] that the mass-transport processes in supported Pt clusters can affect their performance as catalysts. For instance, the mobility of the atoms within the cluster affects both the activation barriers for adsorbate dissociation as well as reaction rate prefactors.[13] In addition, the overall mobility of the cluster as a whole is likely related to nanoparticle coalescence and sintering, phenomena usually associated with the deactivation of the catalysts.[18−20] The computation of these diffusion processes using ab initio MD techniques is computationally very demanding since long simulation runs are needed, using many initial conditions. Therefore, the use of efficient model potentials is an excellent alternative. Here we compute the average diffusion coefficient of the individual Pt atoms, as well as that of the center of coordinates of the cluster (CC) using the Green−Kubo relation[21] between the self-diffusion coefficient and the velocity autocorrelation function (VACF) of the system, given by

$$D = \frac{1}{3N}\int_{t=0}^{\infty}\sum_{i}^{N}\langle v_i(0)\cdot v_i(t)\rangle\, dt \qquad (13)$$

The integral converges rapidly beyond a characteristic correlation time. In practice, this behavior is simulated by averaging the VACF over many intervals and initial conditions, and the integrand dampens to near zero after about 5−10 ps, depending on the temperature.[21] The VACF is a measure of how quickly the system loses the information on its initial conditions. Figure 9 shows the normalized VACF for Pt_{10} as a function of temperature, exhibiting a rapid loss of correlation as the temperature increases.

The Pt and CC self-diffusion coefficients determined from these VACFs are shown in Figure 10, and are in the range expected for liquid diffusion.[22] They can be fit to a simple Arrhenius model for mass-diffusivity $D = D_0 e^{-E_A/k_B T}$ where D_0 is the diffusion coefficient in the limit of infinite temperature, E_A is the effective activation energy for diffusion, and k_B is Boltzmann's constant. This analysis reveals two distinct regimes, separated by a diffusion onset, where diffusion is only measurable above a certain temperature. In the case of the CC diffusion, the onset occurs at 310 K for Pt_{10} and 400 K for Pt_{20}. These values are in good agreement with both the onset of the NTE at 300 and 400 K, and the changes in σ^2_{PtPt} behavior at 330 and 400 K for Pt_{10} and Pt_{20}, respectively. Our initial hypothesis[5] attributed the origin of NTE to a combination of processes, including the "unlocking" of the cluster from the surface, and a consequent change in the internal electronic charge distribution, both of which contributed to the contraction of the bonds. The present results support the structural component of this hypothesis: At low temperature the nanoparticles are locked in position and the Pt layer in contact with the support is forced into forming longer Pt−Pt

DOI: 10.1021/acs.jpcc.6b03074
J. Phys. Chem. C 2016, 120, 14883−14891

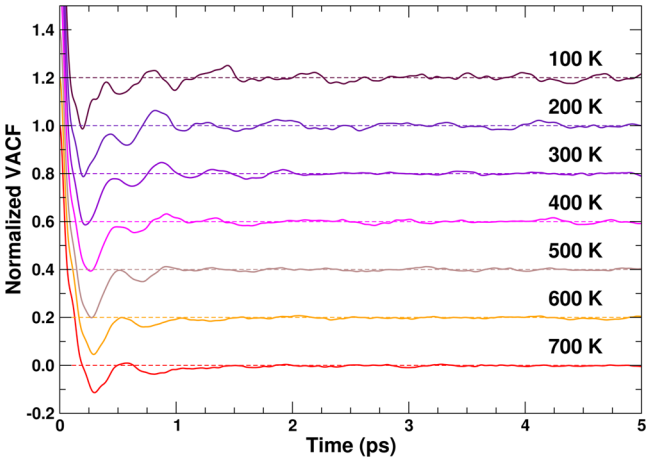

Figure 9. Normalized velocity autocorrelation functions for Pt_{10} as a function of temperature, calculated with the new hybrid SC potential. The VACFs were averaged over both time interval and initial conditions.

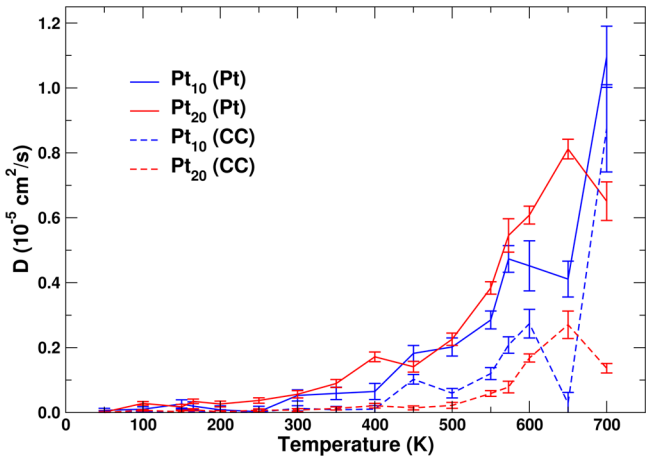

Figure 10. Average atomic (Pt) and cluster center of coordinates (CC) diffusion coefficients for Pt_{10} and Pt_{20} as a function of temperature calculated with the new hybrid SC potential.

bonds. When the cluster becomes mobile at higher temperatures, however, this constraint is released allowing the atoms to form shorter bonds, thus causing the overall observed NTE. The barrier for cluster diffusion is very similar for both Pt_{10} and Pt_{20}, with an estimated value of 0.22 eV. Regarding the fluctuations in charge distribution, we believe our model potential includes these in an effective way given that it was parametrized to reproduce the ab initio results.

The analysis of the Pt diffusion coefficients also reveals diffusion onsets, but at lower temperatures of about 250 K for Pt_{10} and about 320 K for Pt_{20}, with activation energies of ∼0.14 eV in both cases. Although these onsets occur at slightly higher temperatures, they are likely correlated with the onset for decrease in the NN_{Pt} at about 200 K (Figure 7), and the region of positive thermal expansion observed for Pt_{20} below 200−250 K (Figure 6). We believe they are associated with the internal "melting" of the nanoparticles which, atomistically, corresponds to the breaking and reforming of Pt−Pt bonds in the Pt−Pt···Pt ⇌ Pt···Pt−Pt process. To investigate this hypothesis we have computed the rate constant for Pt−Pt bond breaking

$$k_{Pt} = \left\langle \frac{1}{N_{PtPt}} \frac{dN_{PtPt}}{dt} \right\rangle \quad (14)$$

as a function of temperature. Here N_{PtPt} is the number of Pt−Pt bonds in the cluster at a certain time t, where the threshold for considering that a bond is broken is $R_{PtPt} > 3.1$ Å. An equivalent expression can be written for the rate constant for bond formation. Figure 11 shows only the bond breaking rate

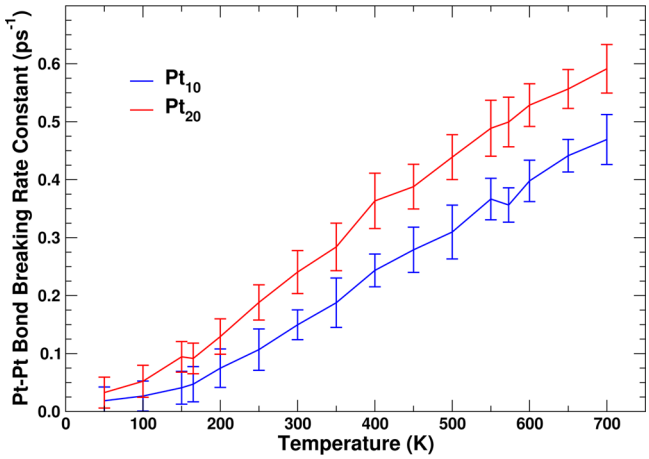

Figure 11. Pt−Pt bond breaking rate constant for Pt_{10} and Pt_{20} as a function of temperature. The Pt−Pt bond formation rate constants are the same within the error of the calculations.

constants. The bond formation rate constants are the same within the error of the calculations, as expected from the symmetric nature of the process. The k_{Pt} can be fitted to an Arrhenius form similarly to the diffusion coefficients. These fits confirm the existence of bond breaking onsets at ∼180 K for both Pt_{10} and Pt_{20}, in reasonable agreement with the low temperature onsets observed for the other properties. The activation energies for the bond-breaking process are ∼0.04 and 0.05 eV for Pt_{10} and Pt_{20}, respectively. These energies are about 3 times smaller than those observed for the Pt diffusion, thus indicating that an effective diffusion step might require more than just a single bond-breaking event.

4. CONCLUSIONS

We have presented a modified, hybrid SC potential to simulate the Pt−Pt interaction in nanoscale clusters in the presence of a model γ-Al_2O_3 support. This hybrid potential permits calculations orders of magnitude faster than currently possible with AIMD. This speedup allows one to probe long-time properties such as diffusion and bond breaking, for which first-principles calculations are prohibitive. By fitting to first-principles DFT/MD calculations as the reference for parametrization, we have been able to include the essential modulation of the Pt−Pt interaction arising from many-body effects induced by the support. Although the parametrization was derived from only one cluster size, we were able to reproduce the DFT/MD results for larger clusters, indicating that the current form of the potential is reasonably transferable. Consequently the model can be of significant value in building models of nanocatalysts for analyzing X-ray spectroscopy experiments, which typically measure global averages. In addition, the efficiency of the calculations allowed us to explore a broad range of temperatures, revealing size-dependent

DOI: 10.1021/acs.jpcc.6b03074
J. Phys. Chem. C 2016, 120, 14883−14891

dynamical changes as the temperature rises. In the case of Pt_{20}, the clusters start in a "frozen" state with normal expansion properties and an intact first shell, until the Pt−Pt bonds start to break at between 170 and 230 K. This initiates a process of internal mass-transfer and diffusion that is associated with a plateau in thermal expansion and a decrease in the number of near-neighbors. At about 400 K, the clusters become "unstuck" from the surface and a process of cluster diffusion begins. This process is associated with the negative thermal expansion as speculated in our original DFT/MD study.[5] Finally, the new parametrization has significant implications for understanding nanocatalysis, where catalytic reactions are often dominated by their low-coordination surface properties. Thus, the new model will facilitate investigations of reaction rates and fluctuating barriers and other nanocluster properties that are currently intractable computationally.[23]

■ ASSOCIATED CONTENT

Supporting Information

The Supporting Information is available free of charge on the ACS Publications website at DOI: 10.1021/acs.jpcc.6b03074.

Figure S1, containing a comparison of pair potentials computed with the SC potentials, and the DFT and CCSD(T) methods. (PDF)

■ AUTHOR INFORMATION

Corresponding Author

*E-mail: fdv@uw.edu. Phone: (1) 206 5439697. Fax: (1) 206 6850635.

Notes

The authors declare no competing financial interest.

■ ACKNOWLEDGMENTS

This work was supported in part by U.S. Department of Energy, Office of Basic Energy Sciences, Catalysis Science Program, Grant No. DE-FG02-03ER15476, with computational support from NERSC, a DOE Office of Science User Facility, under Contract No. DE-AC02-05CH11231. We thank A. Frenkel for many helpful comments. One of us (J.M.M.) is also grateful to REU program directors S. Gupta, A. Garcia, and the staff at the Institute of Nuclear Theory for facilitating this research, with financial support provided by the National Science Foundation.

■ REFERENCES

(1) Schlögl, R.; Abd Hamid, S. B. Nanocatalysis: Mature Science Revisited or Something Really New? *Angew. Chem., Int. Ed.* **2004**, *43*, 1628−1637.

(2) Antos, G.; Aitani, A. *Catalytic Naphtha Reforming*; Chemical Industries Series; Marcel Dekker Inc.: New York, 2004.

(3) Kang, J. H.; Menard, L. D.; Nuzzo, R. G.; Frenkel, A. I. Unusual Non-Bulk Properties in Nanoscale Materials: Thermal Metal-Metal Bond Contraction of g-Alumina-Supported Pt Catalysts. *J. Am. Chem. Soc.* **2006**, *128*, 12068.

(4) Marx, D.; Hutter, J. In *Modern Methods and Algorithms of Quantum Chemistry*; Grotendorst, J., Ed.; Forschungszentrum Jülich: Berlin, 2000; pp 301−449.

(5) Vila, F.; Rehr, J. J.; Kas, J.; Nuzzo, R. G.; Frenkel, A. I. Dynamic Structure in Supported Pt Nanoclusters: Real-time Density Functional Theory and X-ray Spectroscopy Simulations. *Phys. Rev. B: Condens. Matter Mater. Phys.* **2008**, *78*, 121404.

(6) Sutton, A. P.; Chen, J. Long-Range Finnis-Sinclair Potentials. *Philos. Mag. Lett.* **1990**, *61*, 139−146.

(7) Rafii-Tabar, H.; Sulton, A. P. Long-range Finnis-Sinclair Potentials for F.C.C. Metallic Alloys. *Philos. Mag. Lett.* **1991**, *63*, 217−224.

(8) Doye, J. P. K.; Wales, D. J. Global Minima for Transition Metal Clusters Described by SC Potentials. *New J. Chem.* **1998**, *22*, 733−744.

(9) Wikfeldt, K. T.; Batista, E.; Vila, F.; Jónsson, H. A Transferable H_2O Interaction Potential Based on a Single Center Multipole Expansion: SCME. *Phys. Chem. Chem. Phys.* **2013**, *15*, 16542−16556.

(10) Ferrando, R.; Jellinek, J.; Johnston, R. L. Nanoalloys: From Theory to Applications of Alloy Clusters and Nanoparticles. *Chem. Rev.* **2008**, *108*, 845−910.

(11) Nørskov, J.; Jacobsen, K.; Stoltze, P.; Hansen, L. Many-Atom Interactions in Metals. *Surf. Sci.* **1993**, *283*, 277−282.

(12) Vila, F. D.; Rehr, J. J.; Kelly, S. D.; Bare, S. R. Operando Effects on the Structure and Dynamics of Pt_nSn_m/γ-Al_2O_3 from Ab Initio Molecular Dynamics and X-ray Absorption Spectra. *J. Phys. Chem. C* **2013**, *117*, 12446−12457.

(13) Rehr, J. J.; Vila, F. D. Dynamic Structural Disorder in Supported Nanoscale Catalysts. *J. Chem. Phys.* **2014**, *140*, 13470110.1063/1.4869178

(14) Kresse, G.; Furthmüller, J. Efficient Iterative Schemes for Ab Initio Total-Energy Calculations Using a Plane-Wave Basis Set. *Phys. Rev. B: Condens. Matter Mater. Phys.* **1996**, *54*, 11169−11186.

(15) Cheng, H.; Zhu, Y.-A.; Chen, D.; Åstrand, P.-O.; Li, P.; Qi, Z.; Zhou, X.-G. Evolution of Carbon Nanofiber-Supported Pt Nanoparticles of Different Particle Sizes: A Molecular Dynamics Study. *J. Phys. Chem. C* **2014**, *118*, 23711−23722.

(16) Sanchez, S. I.; Menard, L. D.; Bram, A.; Kang, J. H.; Small, M. W.; Nuzzo, R. G.; Frenkel, A. I. The Emergence of Nonbulk Properties in Supported Metal Clusters: Negative Thermal Expansion and Atomic Disorder in Pt Nanoclusters Supported on γ-Al_2O_3. *J. Am. Chem. Soc.* **2009**, *131*, 7040−7054.

(17) Crozier, E.; Rehr, J.; Ingalls, R. *Amorphous and Liquid Systems*; John Wiley & Sons: New York, 1988; Vol. *92*, p 373.

(18) Campbell, C. T.; Parker, S. C.; Starr, D. E. The Effect of Size-Dependent Nanoparticle Energetics on Catalyst Sintering. *Science* **2002**, *298*, 811−814.

(19) Prieto, G.; Zečević, J.; Friedrich, H.; de Jong, K. P.; de Jongh, P. E. Towards Stable Catalysts by Controlling Collective Properties of Supported Metal Nanoparticles. *Nat. Mater.* **2012**, *12*, 34−39.

(20) Hansen, T. W.; DeLaRiva, A. T.; Challa, S. R.; Datye, A. K. Sintering of Catalytic Nanoparticles: Particle Migration or Ostwald Ripening? *Acc. Chem. Res.* **2013**, *46*, 1720−1730.

(21) Allen, M. P.; Tildesley, D. J. *Computer Simulation of Liquids*; Oxford University Press: Oxford, U.K., 1989; p 60.

(22) Cussler, E. Values of Diffusion Coefficients. *Diffusion Mass Transfer in Fluid Systems*; Cambridge University Press: Cambridge, U.K., 1997; pp 117−126.

(23) Timoshenko, J.; Anatoly, I.; Frenkel, A. I. Probing structural relaxation in nanosized catalysts by combining EXAFS and reverse Monte Carlo methods. *Catalysis Today* **2016**.

DOI: 10.1021/acs.jpcc.6b03074
J. Phys. Chem. C 2016, 120, 14883−14891